ARTICLE

Check for updates

Site-specific electronic and magnetic excitations of the skyrmion material Cu_2OSeO_3

Yanhong Gu[1], Yilin Wang[2,5], Jiaqi Lin[2,6], Jonathan Pelliciari [1], Jiemin Li[1], Myung-Geun Han [2], Marcus Schmidt[3], Gabriel Kotliar[2,4], Claudio Mazzoli[1], Mark P. M. Dean [2] & Valentina Bisogni [1✉]

The manifestation of skyrmions in the Mott-insulator Cu_2OSeO_3 originates from a delicate balance between magnetic and electronic energy scales. As a result of these intertwined couplings, the two symmetry-inequivalent magnetic ions, Cu-I and Cu-II, bond into a spin S = 1 entangled tetrahedron. However, conceptualizing the unconventional properties of this material and the energy of the competing interactions is a challenging task due to the complexity of this system. Here we combine X-ray Absorption Spectroscopy and Resonant Inelastic X-ray Scattering to uncover the electronic and magnetic excitations of Cu_2OSeO_3 with site-specificity. We quantify the energies of the $3d$ crystal-field splitting for both Cu-I and Cu-II, fundamental for optimizing model Hamiltonians. Additionally, we unveil a site-specific magnetic mode, indicating that individual spin character is preserved within the entangled-tetrahedron picture. Our results thus provide experimental constraints for validating theories that describe the interactions of Cu_2OSeO_3, highlighting the site-selective capabilities of resonant spectroscopies.

[1] National Synchrotron Light Source II, Brookhaven National Laboratory, Upton, NY 11973, USA. [2] Department of Condensed Matter Physics and Materials Science, Brookhaven National Laboratory, Upton, NY 11973, USA. [3] Max Planck Institute for Chemical Physics of Solids, Nöthnitzer Straße 40, D-01187 Dresden, Germany. [4] Department of Physics and Astronomy, Rutgers University, Piscataway, NJ 08856, USA. [5] Present address: Hefei National Laboratory for Physical Sciences at Microscale, University of Science and Technology of China, Hefei, Anhui 230026, China. [6] Present address: School of Science, Westlake University, Hangzhou 310024 Zhejiang, China. ✉email: bisogni@bnl.gov

Since their first observation in magnetic solids[1,2], skyrmions—nano-sized, topological spin objects—immediately attracted enormous interest, thanks to their unique mobility properties in response to low current and electric fields[3–5]. Skyrmions are consequently appealing for energy-efficient applications and their generation in insulators is furthermore attractive due to reduced heat dissipation and fast switching response. Cu_2OSeO_3 is one of the few known Mott-insulators hosting skyrmions[6–9]. Normally, chiral, noncentrosymmetric, cubic magnetic materials are potential hosts for skyrmions[10], but in the multiferroic Cu_2OSeO_3, the formation of such topological states furthermore arises from the delicate balance between the super-exchange couplings and the Dzyaloshinskii–Moriya (DM) interactions[11–14].

While Cu_2OSeO_3 shares the same $P2_13$ space group as the skyrmion-prototype MnSi[1], the fundamental magnetic unit behind the skyrmion nucleation within the ferrimagnetic phase is believed to be a composite Cu_4 tetrahedron with an effective spin S = 1[11] and involving two differently coordinated Cu ions, Cu-I and Cu-II. Several studies[11–13,15] identified the microscopic interactions between the individual ions within the magnetic building block as crucial to unravel the quantum nature of the skyrmions in Cu_2OSeO_3 and to explain the emergence of other unconventional phases[9,16,17].

As most experimental works focused so far on site-averaged magnetic properties of Cu_2OSeO_3[13,15,18,19], the site-specific magnetic response and the local electronic structure of the Cu 3d valence states remain marginally understood[20,21]. Nonetheless, the latter is fundamentally related to the DM interactions—responsible for the helical order and the skyrmion formation[22]—as they are explained through multi-orbital and multisite hopping paths, involving both Cu-I and Cu-II. On the other hand, the site-specific magnetic response can elucidate the validity of the Cu_4 tetrahedron picture at the microscopic level, exploiting the single spin point of view.

Hence, the complex nature of Cu_2OSeO_3 calls for site-specific magnetic and electronic investigations. These results will build prerequisite information for extracting all the interactions underlying the skyrmion generation in this system—by experimentally validating microscopic theoretical models—ultimately unveiling the real energy balance that stabilizes the skyrmion phase. Such information is crucial for future skyrmion applications, as it promises the possibility for designing optimized materials—i.e., with an extended skyrmion pocket in the magnetic phase diagram—where the key interactions can be tuned either by film thickness, electric field, pressure, or strain[6,8,23,24].

Here, we combine X-ray absorption spectroscopy (XAS) and resonant inelastic X-ray scattering (RIXS) to unveil the electronic and magnetic excitations associated with the two inequivalent Cu sites in the ferrimagnetic phase of Cu_2OSeO_3 ($T_C \simeq 57$ K). Using density functional theory (DFT) and RIXS cross section calculations, we disentangled the resonant energies associated with Cu-I and Cu-II ions. Capitalizing on this finding, we determine the site-specific spectral fingerprints and extract the orbital symmetries and energies of the crystal-field split 3d levels for both Cu-I and Cu-II. Furthermore, we reveal a site-specificity of the medium-energy magnon mode around 35 meV. Our results thus provide an experimental constraint for theories aimed at quantifying the competing energy terms underlying the skyrmion formation. More broadly, this approach can be extended to the design of devices and heterostructures with improved skyrmion properties, highlighting the importance of resonant techniques when dealing with multisite complex systems.

Results and discussion
Soft X-ray resonant spectroscopies of Cu_2OSeO_3. Resonant spectroscopies with their chemical sensitivity provide unique

advantages in the study of multisite compounds. RIXS is furthermore helpful when there is a need to study the valence electronic structure as it probes the charge-neutral, dipole-forbidden, dd-excitations of a system, enabling it to reconstruct its ground state energy levels[25–30]. In particular, for 3d elements, such excitations can be accessed using the L_3 edge resonance in the soft x-ray range, promoting electrons from the $2p_{3/2}$ core states to the 3d valence states. In the present study on Cu_2OSeO_3, we use the Cu L_3 edge at ~930 eV to probe the magnetic Cu ions.

Figure 1a shows the crystallographic unit cell of Cu_2OSeO_3, containing 16 Cu atoms arranged in four tetrahedrons. Each tetrahedron (dashed orange line in Fig. 1a) consists of one Cu-I and three Cu-II ions. Below the ferrimagnetic ordering temperature T_C, the Cu-I spin aligns anti-parallel to the Cu-II spins. As each Cu brings a spin momentum of 1/2, this configuration yields a total spin momentum of S = 1 for the tetrahedron unit. For the XAS and RIXS measurements, we prepared a single crystal with [100] surface normal. The sample orientation used throughout the experiment is displayed in the inset of Fig. 1b.

Figure 1b presents the Cu L_3 XAS spectrum of Cu_2OSeO_3 (blue line) acquired in terms of Total Fluorescence Yield (TFY), at T = 45 K. The line-shape and the peak at 930.9 eV are consistent with previous measurements[31], although our interpretation differs from ref. [20] as explained later on in the text. Since a single Cu $3d^9$ site hosts one hole, its XAS spectrum is expected to be a Lorentzian curve with a 2p core-hole lifetime-dominated
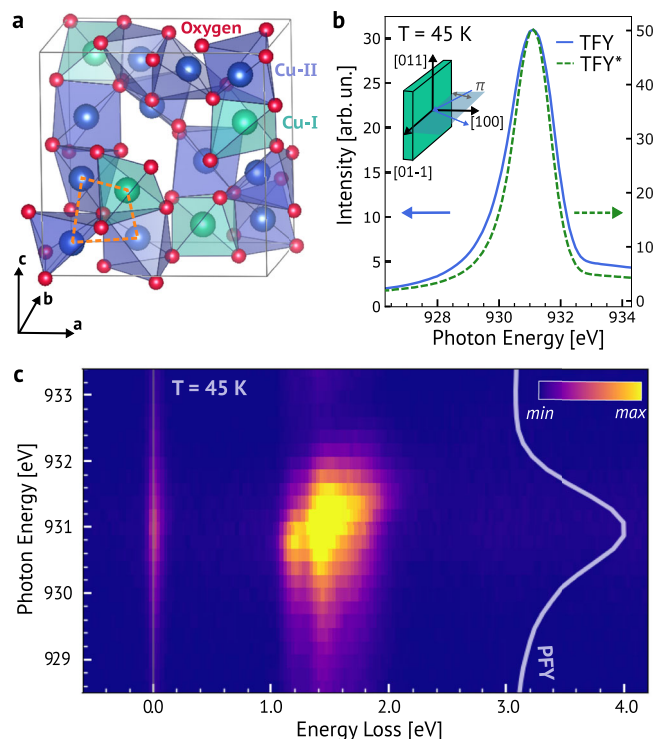

Fig. 1 Overview of the crystal structure, experimental configuration, and Cu L_3 X-ray absorption spectroscopy (XAS) and resonant inelastic X-ray scattering (RIXS) data. a Cu_2OSeO_3 unit cell ($a = 8.925$ Å). The orange dashed line highlights the magnetic tetrahedron unit. **b** Cu L_3 XAS spectrum in terms of total fluorescence yield (TFY), at T = 45 K. TFY* is the spectrum after correction for self-absorption and saturation effects. **c** RIXS energy map with linear color scale for the intensity, also at T = 45 K. The thin solid line displays the partial fluorescence yield (PFY) signal, obtained integrating the RIXS spectra up to 10 eV. The inset in panel **b** displays the sample orientation used for these measurements, with [100] and [01-1] axes lying within the scattering plane. Incoming π polarized x-rays were used for all measurements.

width of 0.3–0.5 eV[32,33]. While the enhanced width of ~1.2 eV and the asymmetric line-shape suggest distinct contributions from the Cu-I and Cu-II sites, we underline that their energy splitting $\Delta E_{CuII-CuI}$ should be intrinsically small. This is supported by TFY* (green dashed line), corrected TFY for self-absorption and saturation effects[34,35], that still displays an asymmetric single-peaked line-shape with ~1 eV large width.

No clear consensus has been reached so far on the value of $\Delta E_{CuII-CuI}$. Previous DFT+U calculations estimated $\Delta E_{CuII-CuI}$ to be ~0.2 eV[21,22], while resonant x-ray scattering proposed $\Delta E_{CuII-CuI}$ to be ~2 eV[20]. Here, we quantify $\Delta E_{CuII-CuI}$ and resolve the $3d$ electronic structure for each Cu site using RIXS at the Cu L_3 edge. The spectra acquired by varying the incident photon energy within the range ~928–933 eV are plotted versus energy loss and gathered in a color map (see Fig. 1c). This displays two main features: the quasi-elastic line around zero-energy loss and a broad multi-peaked structure between 1 and 2 eV. The latter excitations are interpreted as intra-site dd-excitations stemming from the local crystal field in agreement with ellipsometry data[21] and other RIXS measurements on Cu^{2+} systems[26,27].

The fine details of the dd-excitations are shown in Fig. 2a, where the RIXS spectra are presented as a vertical stack for increasing incident photon energy. While the overall intensity evolution of the spectral-weight is due to changing the photon energy across the absorption resonance, the shape evolution between 930.6 and 932 eV highlights the existence of different sets of crystal-field excitations. The excitations pattern originates from the presence of the two inequivalent Cu species, Cu-I and Cu-II, having different oxygen coordination. However, because of the small splitting between Cu-I and Cu-II energy levels as suggested

by the XAS, it is necessary to resort to more involved data analysis for disentangling the site-specific crystal-field excitations and their resonant energies.

Resolving Cu-I and Cu-II electronic structure using DFT and single-ion calculations. Preliminary considerations of the orbital excitations of the two sites can be made by examining the distinct point group symmetries of the crystal field associated with Cu-I, approximately a trigonal bipyramid D_{3h}, and Cu-II, approximately a square pyramid C_{4v}[21,36]. These two symmetries naturally lead to different orbital arrangements[21]. The ground state (GS) orbitals can be identified by referring to the local Cartesian axis (see Fig. 2b) that minimizes the Cu-O distance (z_1 for Cu-I yielding a d_{z^2} GS, and x_2/y_2 for Cu-II yielding a $d_{x^2-y^2}$ GS), in agreement with refs. [21,22]. To obtain an estimate of the site-specific orbital character and energy of the crystal-field split $3d$ levels in Cu_2OSeO_3, we perform DFT combined with Wannier90 calculations. Details on the DFT part can be found in Supplementary Note 1. Tight binding (TB) Hamiltonians $\hat{H}_{Cu-I}^{CF}$ and $\hat{H}_{Cu-II}^{CF}$ consisting of $3d$ orbitals from four Cu-I sites and from twelve Cu-II sites are then formulated. From the calculated $3d$ energies, we can directly extract the crystal-field excitation energies for each Cu site and use them as a guide to fit the experimental data. Together with the schematics of Fig. 2b, we thus expect two dd-excitations for Cu-I, labeled as E1 and E3, and four dd-excitations for Cu-II, labeled as E2, E4, E5, and E6. Note that E0 corresponds to the zero-energy transition, obtained when the initial and final $3d$ levels coincide.

To address the Cu-I and Cu-II resonant energies as well as their respective orbital energies, we simulate XAS and RIXS spectra based on a single-atom model using the EDRIXS code[37]. Details are collected in Supplementary Note 2. The intensity of the calculated RIXS spectra accounts for all atoms within the unit cell, neglecting interference effects between them. Furthermore, the experimental geometry and the incoming polarization projections are included as well. By using the theoretical energies for the dd-excitations (see Supplementary Table 3) and the RIXS intensity obtained from the atomic model calculations, we can simulate the RIXS spectra associated with each Cu species, see Fig. 2c for Cu-I and Fig. 2d for Cu-II. We performed then a constrained fit where the integrated intensity of each dd transition is fixed to the theoretical model while their energy and width are allowed to vary. As detailed in the Supplementary Note 3, we use the following model to fit the data:

$$I_{RIXS}^{total} = A^{CuI} \cdot \tilde{I}_{RIXS}^{CuI} + A^{CuII} \cdot \tilde{I}_{RIXS}^{CuII} \tag{1}$$

where $A^{CuI/II}$ are the site-specific amplitudes at each incident energy and $\tilde{I}_{RIXS}^{CuI/II}$ are the site-specific area-normalized theoretical RIXS spectra.

The fitted spectra are presented in Figs. 3a–p, where each panel refers to specific incident energy and displays the raw data (open dots), the fitted Gaussian components for each dd-excitations (solid filling in aquamarine color for Cu-I and purple color for Cu-II), and their sum (pink solid line). Figure 3q–r summarize the fitted dd-excitation center positions, corresponding to the E1–E6 values. Notably, the extracted peak positions are reasonably constant across the scanned incident energy range, validating the reliability of the fitting model, while their averages and errors are summarized in Table 1.

From these results, we conclude that the experimental dd-excitation energies are well reproduced by the eigenvalues of the $\hat{H}_{Cu-I}^{CF}$ and $\hat{H}_{Cu-II}^{CF}$ Hamiltonians (within 10–20%), and confirm that the effective D_{3h} symmetry for Cu-I ion and the distorted C_{4v} symmetry for Cu-II ion are good approximations for the real material despite small distortions from these idealized symmetries.
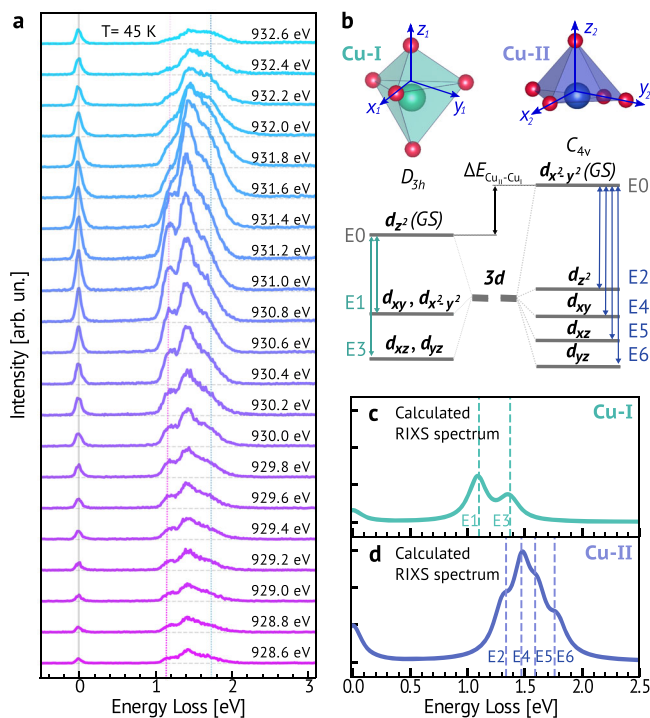

Fig. 2 dd-excitations of Cu-I and Cu-II. a Resonant inelastic X-ray scattering (RIXS) spectra as a function of incident photon energy, for a selected incident energy range: 928.6 to 932.6 eV. **b** Crystal-field splittings of the Cu-I (Cu-II) $3d$ orbitals in D_{3h} (C_{4v}) point group symmetry, respectively. The $3d$ orbitals are defined with respect to the local Cartesian coordinates indicated in blue. The vertical arrows labeled E1 to E5 associate the dd-excitations with the respective initial and final $3d$ levels. **c**, **d** Calculated RIXS responses for the individual Cu-I and Cu-II ions.
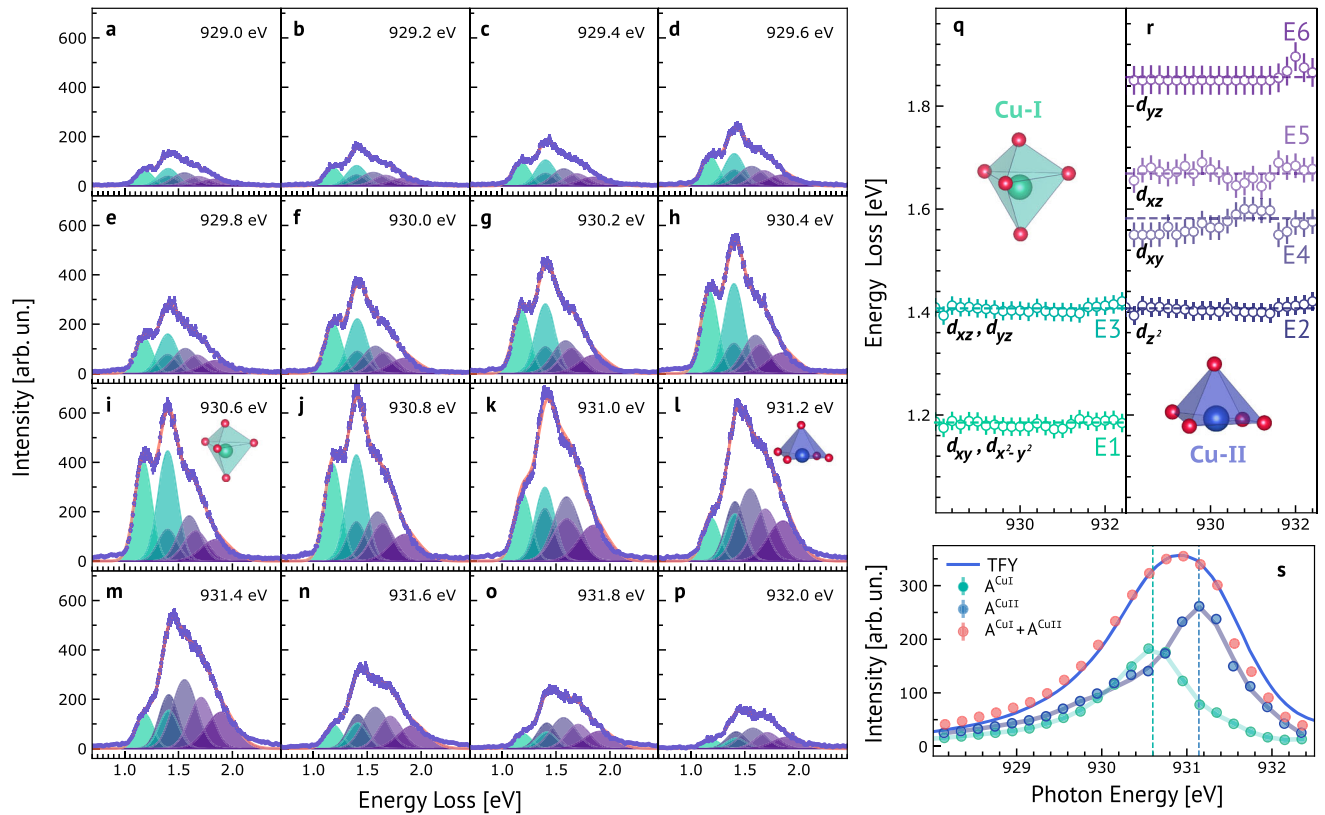
Fig. 3 Analysis of *dd*-excitations in Cu$_2$OSeO$_3$. a–p Resonant inelastic X-ray scattering (RIXS) spectra (dots), in the 0.8–2.5 eV region, as a function of incident energy across the Cu L$_3$ edge. The error bars are defined assuming a Poisson distribution of the single-photon counted events. The fitted components are colored in aquamarine for the Cu-I *dd*-excitations (E1 and E3), and in purple for the Cu-II *dd*-excitations (E2, E4, E5, and E6). The sum of the fitted components is represented as a pink, thick solid line. **q, r** Summary of the fitted *dd*-excitation energies across the Cu L$_3$ edge, with the assigned orbital character following density functional theory (DFT) calculations. **s** Site-resolved *dd*-excitation amplitudes A^{CuI} (aquamarine dots) and A^{CuII} (blue dots). The error bars, extracted from the fitting through the error propagation method, are contained within the marker size. The smoothed lines underneath are a guide for the eyes. The sum of the A^{CuI} and A^{CuII} amplitudes is displayed by the pink dots. A rescaled total fluorescence yield (TFY) profile is plotted in the same figure using a blue solid line. Vertical dotted lines mark the resonant energy extracted for Cu-I ion at 930.6 eV and Cu-II ion at 931.15 eV.

Table 1 *dd*-excitation energies in Cu$_2$OSeO$_3$.

Site	Excitation	Energy [eV]
Cu-I	E1	1.18 ± 0.01
	E3	1.40 ± 0.01
Cu-II	E2	1.4 ± 0.01
	E4	1.57 ± 0.01
	E5	1.67 ± 0.01
	E6	1.86 ± 0.01

Energies of the Cu-I and Cu-II *dd*-excitations, extracted from the fit of the resonant inelastic X-ray scattering (RIXS) measurements. The errors are defined as the standard deviation associated with the least square fit results.

Furthermore, by plotting the A^{CuI} and A^{CuII} amplitudes as a function of the incident photon energy, we obtain the experimental resonant profiles for Cu-I and Cu-II sites (see Fig. 3s). By summing the A^{CuI} and A^{CuII} amplitudes across the Cu L$_3$ edge (pink dots in Fig. 3s) we can well reproduce the XAS of Cu$_2$OSeO$_3$ (blue solid line): this good agreement corroborates the consistency of the analysis. After extracting the respective maxima position from the A^{CuI} (~930.6 eV) and A^{CuII} (~931.15 eV) profiles, we can additionally quantify $\Delta E_{CuII-CuI}$ ~0.55 ± 0.05 eV, as the energy difference between the Cu-I and Cu-II resonances. This value is a bit larger than our theoretical

estimate (~0.33 eV, refer to Supplementary Note 1) and previous DFT+U work[21,22], while it strongly differs from the value reported in ref. [20], ~2 eV. Our result finally legitimates the approximation of neglecting interference effects between the two inequivalent Cu species, since $\Delta E_{CuII-CuI} \gtrsim \Gamma_{CuL}$.

Site-dependent magnetic excitations. The magnetic properties of Cu$_2$OSeO$_3$, as well as the magnon modes, have been explained so far as emanating from the effective S = 1 Cu$_4$ tetrahedra[11–13,15,18], rather than from individual Cu spins, yielding the definition of "entangled-tetrahedron ground state". However, some discrepancies between the Cu$_4$ tetrahedra model and the spin excitations have been reported in ref. [38]. Benefiting from the unique site sensitivity offered by RIXS as demonstrated above, we investigate the site-dependence of the magnon modes in Cu$_2$OSeO$_3$, to assess possible contributions of the two inequivalent Cu sites into the spin excitations improving our current understanding of this complex system.

The magnon spectrum of Cu$_2$OSeO$_3$ has been studied so far by several techniques, e.g., inelastic neutron scattering, Raman, Infrared, ESR, and THz spectroscopy[13,15,18,39,40]. These results consistently reported (i) inter-tetrahedron ferromagnons below 15 meV; (ii) intra-tetrahedron, medium-energy magnon branches between 30–40 meV; (iii) high-energy (>50 meV) phonon modes and multi-magnons. In Fig. 4 we display high-resolution RIXS
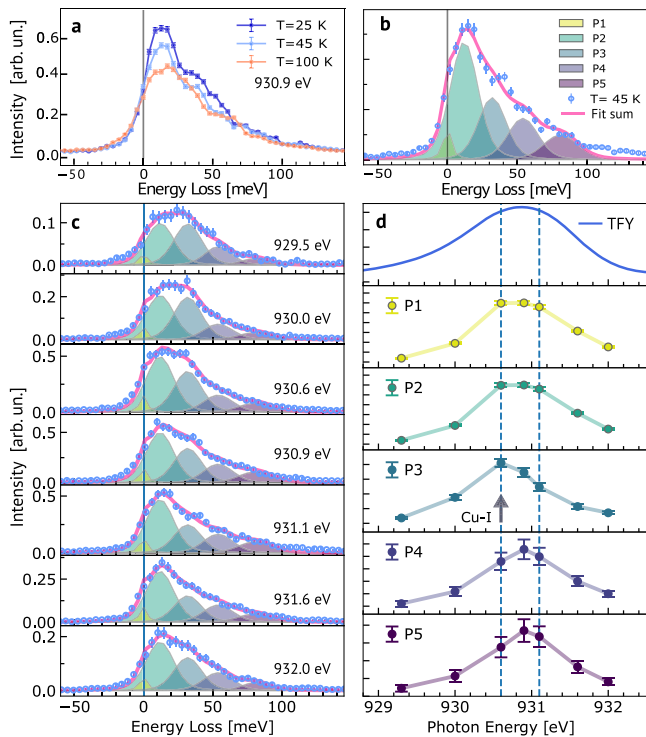
Fig. 4 Magnetic excitations in Cu₂OSeO₃. a High-resolution resonant inelastic X-ray scattering (RIXS) spectra measured at an incident energy of 930.9 eV, **q** = [1.3,0,0] r.l.u. for T = 27, 45, and 100 K, with π polarized light. The zero-energy was determined with reference to a carbon tape placed on the sample. **b** Fitting analysis of the 45 K RIXS spectrum, using five Gaussian peaks with a fixed width, fixed center position (allowing ±5% variation w.r.t. the values presented in the main text), and free amplitude. Raw data were displayed as open dots. The fitting sum is the solid line. The error bars are defined assuming a Poisson distribution of the single-photon counted events. **c** Repeating the fitting analysis for all RIXS spectra measured across the Cu L_3 resonance. **d** Summary of the integrated intensity for each fitting component, as a function of the incident photon energy (dot symbols). The error bars are extracted from the fitting, through the error propagation method. The smoothed lines underneath are a guide for the eyes. The Cu L_3 absorption spectrum is reproduced on top to ease the comparison.

spectra of Cu₂OSeO₃ at **q** = [1.3,0,0] r.l.u., measured at the Cu L_3 edge. From Fig. 4a, a long tail up to 100 meV can be observed. With reference to the magnon dispersion measured by inelastic neutron scattering[15,18], at **q** = [1.3,0,0] r.l.u., we expect the first component around 12 meV from the ferromagnon mode, a second one around 35 meV from the medium-energy magnon branches. A phonon mode around 54 meV is furthermore expected, consistently with Raman and Infrared data[39,40]. Moreover, we attribute the high-energy spectral-weight around 70–80 meV to multi-magnons. This assignment is further supported by the temperature dependence of Fig. 4a[41], where the spectral-weight of the magnetic components is enhanced below T_C, up to 100 meV. Using resolution limited Gaussian peaks (FWHM = 30 meV) for fitting the elastic peak (P1, 0 meV), the ferromagnon (P2, 12 meV), the medium-energy magnon (P3, 35 meV), the phonon (P4, 54 meV) and a wider Gaussian for high-energy multi-magnon component (P5, 80 meV, FWHM = 40 meV), we can accurately reproduce the RIXS spectrum at T = 45 K, see Fig. 4b.

To investigate the site-dependent character of the magnetic excitation, we collected RIXS spectra as a function of incident photon energy across the Cu L_3 edge, while leaving **q**

unchanged. The resulting data are presented in Fig. 4c. As expected, an overall amplitude renormalization of the whole spectrum takes place due to the absorption effect. However, by tracking the individual P1-P5 components through the fitting analysis, we can extract the intensity behavior for each individual excitation as a function of the photon energy, see Fig. 4d. The intensity profile of the elastic peak P1, the ferromagnon mode P2, the phonon mode P4, and the multi-magnon mode P5 track well with the TFY absorption profile (peaked at ~903.9 eV), within the error bars. This result suggests these modes do not have any specific or noticeable Cu-site-dependence. Interestingly, instead, the intensity profile of the medium-energy magnon mode P3 displays a pronounced resonance at the Cu-I sites, ~930.6 eV, clearly standing out beyond the error-bar scale. We interpret this peculiar behavior considering the 35 meV component of the RIXS spectra dominated by magnon modes with B and C character[12,13]: these intra-tetrahedron modes correspond to rotating the Cu-I minority spins through the J_S^{AF} interaction, while leaving the Cu-II spins unaltered. Hence, our result highlights that individual Cu spin character persists in the medium-energy magnon modes, simultaneously with the entangled-tetrahedron nature reported so far for the magnetic excitations of Cu₂OSeO₃[11,12]. This finding recalls the magnetic dual nature proposed for MnSi[42], thus highlighting the complexity of these systems.

Conclusions
By combining resonant spectroscopies, DFT, and single-ion calculations, we elucidated the electronic and magnetic excitations of the multisite skyrmion material Cu₂OSeO₃. We identified the L_3 resonant energies for Cu-I and Cu-II ionic species present in this system. With this unique information at hand, we revealed the site-resolved $3d$ electronic structure in terms of crystal-field splittings, and moreover, the difference between the Cu-I and Cu-II ground state energies of about 0.55 eV. Due to the difficulty in accurately calculating these quantities for strongly correlated electron systems, our work provides theorists with an experimental benchmark for fine-tuning microscopic models of Cu₂OSeO₃, hence for extrapolating the competing energy terms, i.e., hopping, exchange integrals and DM interactions. Furthermore, we revealed an unexpected site-dependent character (Cu-I) for the medium-energy magnon branch: this result demonstrates that individual spin character is preserved in specific magnon modes, suggesting that local spin behavior coexists with the entangled nature of the magnetic ground state, explained by means of S = 1 tetrahedra rather than single spins.

More broadly, as the magnetism in Cu₂OSeO₃ is determined by the competition between several interactions (super-exchange interactions, DM interactions, and crystal-anisotropy stemming from the spin–orbit interactions), our results on site-specific magnetic and electronic ground state excitations should be regarded as a prerequisite for validating future and past theoretical models of Cu₂OSeO₃ dedicated to the microscopic understanding of e.g., the skyrmion phase, the magnetic chirality, and the multiferroicity.

Finally, our finding overall highlights the complexity of this skyrmion material and, at the same time, the relevance of using advanced spectroscopies to reveal site-specific information. The method presented here can be extended to thin films and heterostructures of Cu₂OSeO₃ as well as devices (e.g., under the application of electric field) to elucidate the evolution of the site-specific excitations, and thus of the energy balance between the interactions contributing to the skyrmion formation.

Methods

Sample details. Single crystalline Cu_2OSeO_3 was prepared by the chemical vapor transport method[9,15]. A Curie temperature of $T_C \simeq 57$ K was extracted from the sample used in this study, in line with ref. [43].

XAS and RIXS measurements. The XAS and RIXS experiments were performed at the SIX 2-ID beamline of NSLS-II[44]. The XAS data of Fig. 1b was measured in total fluorescence yield (TFY), at an incident angle of $\theta_{in} = 20°$. The energy resolution and experimental geometry used for the RIXS measurements were: $\Delta E = 50$ meV (FWHM) and $\theta_{in} = 20°/2\Theta = 90°$ for the crystal-field study; $\Delta E = 30$ meV (FWHM) and $\theta_{in} = 75°/2\Theta = 150°$ for the spin excitation study. All the measurements used π-polarized x-ray photons.

Calculations. Details about the DFT and single-ion calculations are available respectively in Supplementary Notes 1, 2.

Data availability

Data that support the findings of this study are available upon reasonable request from the corresponding authors.

References

1. Mühlbauer, S. et al. Skyrmion lattice in a chiral magnet. *Science* **323**, 915–919 (2009).
2. Yu, X. Z. et al. Real-space observation of a two-dimensional skyrmion crystal. *Nature* **465**, 901–904 (2010).
3. Nagaosa, N. & Tokura, Y. Topological properties and dynamics of magnetic skyrmions. *Nat. Nanotechnol.* **8**, 899–911 (2013).
4. Finocchio, G., Büttner, F., Tomasello, R., Carpentieri, M. & Kläui, M. Magnetic skyrmions: from fundamental to applications. *J. Phys. D Appl. Phys.* **49**, 423001 (2016).
5. Fert, A., Reyren, N. & Cros, V. Magnetic skyrmions: advances in physics and potential applications. *Nat. Rev. Mater.* **2**, 17031 (2017).
6. Seki, S., Yu, X. Z., Ishiwata, S. & Tokura, Y. Observation of skyrmions in a multiferroic material. *Science* **336**, 198–201 (2012).
7. Seki, S. et al. Formation and rotation of skyrmion crystal in the chiral-lattice insulator Cu_2OSeO_3. *Phys. Rev. B* **85**, 220406 (2012).
8. Ruff, E., Lunkenheimer, P., Loidl, A., Berger, H. & Krohns, S. Magnetoelectric effects in the skyrmion host material Cu_2OSeO_3. *Sci. Rep.* **5**, 15025 (2015).
9. Qian, F. et al. New magnetic phase of the chiral skyrmion material Cu_2OSeO_3. *Sci. Adv.* **4**, eaat7323 (2018).
10. Lohani, V., Hickey, C., Masell, J. & Rosch, A. Quantum skyrmions in frustrated ferromagnets. *Phys. Rev. X* **9**, 041063 (2019).
11. Janson, O. et al. The quantum nature of skyrmions and half-skyrmions in Cu_2OSeO_3. *Nat. Commun.* **5**, 5376 (2014).
12. Romhányi, J., van den Brink, J. & Rousochatzakis, I. Entangled tetrahedron ground state and excitations of the magnetoelectric skyrmion material Cu_2OSeO_3. *Phys. Rev. B* **90**, 140404 (2014).
13. Ozerov, M. et al. Establishing the fundamental magnetic interactions in the chiral skyrmionic Mott insulator Cu_2OSeO_3 by terahertz electron spin resonance. *Phys. Rev. Lett.* **113**, 157205 (2014).
14. Zhang, L.-C. et al. Magnonic Weyl states in Cu_2OSeO_3. *Phys. Rev. Res.* **2**, 013063 (2020).
15. Portnichenko, P. Y. et al. Magnon spectrum of the helimagnetic insulator Cu_2OSeO_3. *Nat. Commun.* **7**, 10725 (2016).
16. White, J. S. et al. Electric-field-driven topological phase switching and skyrmion-lattice metastability in magnetoelectric Cu_2OSeO_3. *Phys. Rev. Appl.* **10**, 014021 (2018).
17. Aqeel, A. et al. Microwave spectroscopy of the low-temperature skyrmion state in Cu_2OSeO_3. *Phys. Rev. Lett.* **126**, 017202 (2021).
18. Tucker, G. S. et al. Spin excitations in the skyrmion host Cu_2OSeO_3. *Phys. Rev. B* **93**, 054401 (2016).
19. Versteeg, R. B., Boguschewski, C., Becker, P. & van Loosdrecht, P. H. M. Inelastic light scattering in the spin cluster Mott insulator Cu_2OSeO_3. *Phys. Rev. B* **100**, 224426 (2019).
20. Langner, M. et al. Coupled skyrmion sublattices in Cu_2OSeO_3. *Phys. Rev. Lett.* **112**, 167202 (2014).
21. Versteeg, R. B. et al. Optically probed symmetry breaking in the chiral magnet Cu_2OSeO_3. *Phys. Rev. B* **94**, 094409 (2016).
22. Yang, J. H. et al. Strong Dzyaloshinskii-Moriya interaction and origin of ferroelectricity in Cu_2OSeO_3. *Phys. Rev. Lett.* **109**, 107203 (2012).
23. Deng, L. et al. Room-temperature skyrmion phase in bulk Cu_2OSeO_3 under high pressures. *Proc. Natl Acad. Sci. USA* **117**, 8783–8787 (2020).
24. Burn, D. M. et al. Field and temperature dependence of the skyrmion lattice phase in chiral magnet membranes. *Phys. Rev. B* **101**, 014446 (2020).
25. Ament, L. J. P., van Veenendaal, M., Devereaux, T. P., Hill, J. P. & van den Brink, J. Resonant inelastic x-ray scattering studies of elementary excitations. *Rev. Mod. Phys.* **83**, 705 (2011).
26. Sala, M. M. et al. Energy and symmetry of dd excitations in undoped layered cuprates measured by Cu L_3 resonant inelastic x-ray scattering. *N. J. Phys.* **13**, 043026 (2011).
27. Bisogni, V. et al. Orbital control of effective dimensionality: from spin-orbital fractionalization to confinement in the anisotropic ladder system $CaCu_2O_3$. *Phys. Rev. Lett.* **114**, 096402 (2015).
28. Elnaggar, H. et al. Magnetic contrast at spin-flip excitations: an advanced X-ray spectroscopy tool to study magnetic-ordering. *ACS Appl. Mater. interfaces* **11**, 36213–36220 (2019).
29. Lebert, B. W. et al. Resonant inelastic x-ray scattering study of α-$RuCl_3$: a progress report. *J. Phys.: Condens. Matter* **32**, 144001 (2020).
30. Occhialini, C. A. et al. Local electronic structure of rutile RuO_2. *Phys. Rev. Res.* **3**, 033214 (2021).
31. Zhang, S. L. et al. Resonant elastic x-ray scattering from the skyrmion lattice in Cu_2OSeO_3. *Phys. Rev. B* **93**, 214420 (2016).
32. Krause, M. O. & Oliver, J. H. Natural widths of atomic K and L levels, K alpha X-ray lines and several KLL Auger lines. *J. Phys. Chem. Ref. Data* **8**, 329–338 (1979).
33. Bisogni, V. et al. Femtosecond dynamics of momentum-dependent magnetic excitations from resonant inelastic x-ray scattering in $CaCu_2O_3$. *Phys. Rev. Lett.* **112**, 147401 (2014).
34. Haskel, D. FLUO: correcting XANES for self-absorption in fluorescence measurements. Computer program and documentation [online]. http://www.aps.anl.gov/xfd/people/haskel/fluo.html (1999).
35. Tröger, L. et al. Full correction of the self-absorption in soft-fluorescence extended x-ray-absorption fine structure. *Phys. Rev. B* **46**, 3283–3289 (1992).
36. Bos, J.-W., Colin, C. V. & Palstra, T. T. M. Magnetoelectric coupling in the cubic ferrimagnet Cu_2OSeO_3. *Phys. Rev. B* **78**, 094416 (2008).
37. Wang, Y. L., Fabbris, G., Dean, M. P. M. & Kotliar, G. EDRIXS: an open source toolkit for simulating spectra of resonant inelastic x-ray scattering. *Computer Phys. Commun.* **243**, 151–165 (2019).
38. Tucker, G. S. et al. Spin excitations in the skyrmion host cu2oseo3. *Phys. Rev. B* **93**, 054401 (2016).
39. Gnezdilov, V. P. et al. Magnetoelectricity in the ferrimagnetic Cu_2OSeO_3: symmetry analysis and Raman scattering study. *Low. Temp. Phys.* **36**, 550–557 (2010).
40. Miller, K. H. et al. Magnetodielectric coupling of infrared phonons in single-crystal Cu_2OSeO_3. *Phys. Rev. B* **82**, 144107 (2010).
41. Ellis, D. S. et al. Magnetic nature of the 500 meV peak in $La_{2-x}Sr_xCuO_4$ observed with resonant inelastic x-ray scattering at the CuK-edge. *Phys. Rev. B* **81**, 085124 (2010).
42. Yaouanc, A. et al. Dual nature of magnetism in MnSi. *Phys. Rev. Res.* **2**, 013029 (2020).
43. Wu, H. C. et al. Physical pressure and chemical expansion effects on the skyrmion phase in Cu_2OSeO_3. *J. Phys. D: Appl. Phys.* **48**, 475001 (2015).
44. Dvorak, J., Jarrige, I., Bisogni, V., Coburn, S. & Leonhardt, W. Towards 10 meV resolution: the design of an ultrahigh resolution soft X-ray RIXS spectrometer. *Rev. Sci. Instrum.* **87**, 115109 (2016).

Acknowledgements

Author contributions

V.B. conceived the project, with input from M.P.M.D., M.-G.H., and C.M.; M.P.S. grew and characterized the sample. V.B., M.P.M.D., Y.G., J.Lin, J. Li, and J.P. performed the XAS and RIXS experiments. V.B. analysed and interpreted the data with the help of M.P.M.D., Y.G., J.Lin, C.M., and J.P; Y.W. and M.P.M.D. performed the theory calculations, with help from G.K.; V.B and Y.G. wrote the manuscript with input from all the authors.

Competing interests

The authors declare no competing interests.

Additional information

Supplementary information The online version contains supplementary material available at https://doi.org/10.1038/s42005-022-00934-y.

Correspondence and requests for materials should be addressed to Valentina Bisogni.

Peer review information *Communications Physics* thanks the anonymous reviewers for their contribution to the peer review of this work.

Reprints and permission information is available at http://www.nature.com/reprints

Publisher's note Springer Nature remains neutral with regard to jurisdictional claims in published maps and institutional affiliations.